Complete characterization of the constrained geometry bimolecular reaction $O(^1D)+N_2O \rightarrow NO+NO$ by three-dimensional velocity map imaging

Niels Gödecke,[1] Christof Maul,[1,a)] Alexey I. Chichinin,[2] Sebastian Kauczok,[1] and Karl-Heinz Gericke[1]
[1]*Institut für Physikalische und Theoretische Chemie, Technische Universität Braunschweig, Braunschweig, Germany*
[2]*Institute of Chemical Kinetics and Combustion, Russian Academy of Sciences, Novosibirsk, Russia*

(Received 23 April 2009; accepted 14 July 2009; published online 5 August 2009)

The bimolecular reaction $O(^1D)+N_2O \rightarrow NO+NO$ was photoinitiated in the $(N_2O)_2$ dimer at a wavelength of 193 nm and was investigated by three-dimensional (3D) velocity map imaging. State selective 3D momentum vector distributions were monitored and analyzed. For the first time, kinetic energy resolution and stereodynamic information about the reaction under constrained geometry conditions is available. Directly observable NO products exhibit moderate vibrational excitation and are rotationally and translationally cold. Speed and spatial distributions suggest a pronounced backward scattering of the observed products with respect to the direction of motion of the $O(^1D)$ atom. Forward scattered partner products, which are not directly detectable are also translationally cold, but carry very large internal energy as vibration or rotation. The results confirm and extend previous studies on the complex initiated reaction system. The restricted geometry of the van der Waals complex seems to favor an abstraction reaction of the terminal nitrogen atom by the $O(^1D)$ atom, which is in striking contrast to the behavior observed for the unrestricted gas phase reaction under bulk conditions. © *2009 American Institute of Physics*. [DOI: 10.1063/1.3194292]

I. INTRODUCTION

Three-dimensional (3D) velocity map imaging is a powerful tool for the complete characterization of the dynamics of chemical elementary processes such as photodissociations or bimolecular reactions.[1] It relies on the simultaneous determination of the full 3D momentum vector distribution of reaction products and has successfully been applied to a number of photodissociation and photoionization processes.[2–11] In this work we report the first application of this technique for the complete characterization of a bimolecular reaction.

The reaction

$$O(^1D) + N_2O(X\ ^1\Sigma^+) \rightarrow NO(X\ ^2\Pi) + NO(X\ ^2\Pi) \qquad (1)$$

has extensively been studied in the gas phase and initiated from the $(N_2O)_2$ dimer. It is of utmost importance for atmospheric chemistry since it is the main source of stratospheric nitric oxide (NO), which reacts very efficiently with ozone.[12]

There are numerous gas phase studies of reaction (1) performed under bulk conditions at room temperature. Goldstein *et al.*[13] observed vibrational excitation of NO until $v=11$ employing (1+1) resonance enhanced multiphoton ionization (REMPI) for the detection of NO. Later, the vibrational population of NO was determined to decrease monotonically from $v=0$ to $v=14$.[14–16] Simons and co-workers[17–19] studied the stereodynamics of the reaction by laser induced fluorescence (LIF) and observed vibrational excitation of NO up to $v=18$. Kajimoto and co-workers[15,20] performed LIF studies with isotopically labeled precursor molecules to distinguish between the newly formed and the old NO bonds. Although the vibrational distribution of the new NO was found to be more excited than that of the old NO, their vibrational populations are not significantly different. Rotational and translational temperatures are large (10 000 and 13 000 K) and agree with statistical models.[21,22] Reports on an inverted vibrational distribution and a low rotational temperature for $v=0$ are likely to be erroneous.[18,19,23]

Earlier, Kajimoto and co-workers[24,25] had initiated reaction (1) in the $(N_2O)_2$ dimer by 193 nm photolysis of isotopically labeled N_2O and detected the NO reaction product by LIF in order to characterize its vibrational and rotational populations. Results differ significantly from those of the bulk reaction. Excitation of NO up to $v=7$ was monitored, which was characterized by a bimodal distribution and very low rotational temperatures between 60 and 100 K, from which it was concluded that the reaction proceeds by abstraction of the terminal nitrogen by the oxygen atom.

The $^1A'$ ground state potential energy surface of the $O(^1D)+N_2O(^1\Sigma^+)$ system was studied by several groups.[26–34] The difference in the outcomes of the bulk reaction and of the dimer initiated reaction is striking. The bulk reaction produces fast and highly rotationally excited NO products, and no significant difference between old and new NO products is observed. For the dimer initiated reaction, there exists only one detailed study, which was performed two decades ago, in which moderate vibrational excitation was reported, whereas rotational excitation was very small. Translational excitation and stereodynamics of the dimer initiated reaction have not yet been studied.

a)Electronic mail: c.maul@tu-braunschweig.de.

Therefore the goal of this work is to completely characterize the mechanism of reaction (1) initiated in the van der Waals complex $(N_2O)_2$. To this end one needs to simultaneously determine the quantum state population, the kinetic energy, and the angular distribution of the NO reaction products, a task which is ideally suited for our newly developed 3D velocity map imaging machine.[1] The partitioning of the reaction energy onto the products together with the knowledge of the angular momentum distribution allows one to draw conclusions on the reaction mechanism accounting for the restrained geometry of the system.

II. EXPERIMENTAL

Detailed descriptions of the experimental setup have previously been published.[1,35–37] Briefly, it consists of a combination of a home-built single-field time-of-flight (TOF) mass spectrometer and a position sensitive detector (PSD) based on a delay line (Roentdek).[38–40] The spectrometer was evacuated to a base pressure of about 10^{-7} mbar by a turbo molecular pump system. Pure N_2O or N_2O seeded in helium or in argon was expanded into the TOF region of the vacuum chamber in a supersonic jet produced by a pulsed nozzle (General Valve Series 9). Typically, molecules are cooled to temperatures of 6 K, as was determined in independent measurements of NO samples.

The dissociation of N_2O was performed by 193 nm radiation of an ArF excimer laser (Coherent Optex 3) with pulse duration of typically 10 ns and pulse energy that could be varied between 1 and 5 mJ. The dissociation laser radiation was polarized with more than 95% purity by passing the laser beam through a 10 plate stack of CaF_2 windows tilted at the Brewster angle. The dissociation laser beam perpendicularly intersected the molecular beam (MB) onto which it was mildly focused by the action of a 450 mm lens. NO product molecules in their electronic ground state ($X\ ^2\Pi_\Omega$, v'', J'') were state-selectively detected by (1+1)-REMPI using the $A\ ^2\Sigma^+$ Rydberg state as resonant intermediate.[41] The detection was performed using the frequency doubled output of a dye laser (Coherent, Scanmate 2), which counterpropagated the dissociation laser beam. The dye laser was pumped by a neodymium-doped yttrium aluminum garnet laser (Coherent, Infinity 40–100) and was operated with Coumarin 47 or with Coumarin 102, depending on the desired wavelength range. The polarization of the detection laser was purified by a Rochon polarizer, and the plane of polarization could be rotated by a $\lambda/2$ wave plate. The dye laser beam was focused by a 300 mm lens onto the MB. The overlap of the two laser foci was optimized by adjusting the position of one of the lenses, which was mounted to two computer controlled linear translation stages.

NO^+ ions were detected by double stage multichannel plates forming the first part of the PSD. The integration of an ionic lens into the acceleration region of the TOF spectrometer of the 3D velocity map imaging setup has greatly enhanced the spatial resolution of the PSD.[1] The delay-line anode introduced right behind the multichannel plates allowed us to monitor all three components of the momentum vector from the measured position of the particle on the detector and its arrival time. Thus, in our experiments the full 3D velocity distribution was observed and the complete information about the speed distribution and the spatial anisotropy of the process was obtained.[1]

The pulse energy of the analyzing was typically kept at 50 μJ or below in order to avoid space charge and saturation effects. Although the delay line PSD is multihit capable, an average count rate of ca. 1 count per laser shot was aimed for which guarantees best image quality. Typical acquisition times at a laser repetition rate of 10 Hz were of the order of 1 h, during which between 10^4 and 10^5 events were accumulated in one image.

Polarization effects were carefully studied for both laser beams. Other than in two-dimensional (2D) imaging experiments, changes are neither expected nor observed for the simultaneous rotation of the polarization vectors of both laser beams with respect to the spectrometer axis, since this operation only rotates the 3D momentum vector distribution in the laboratory coordinates. Therefore, the experimental confirmation of identical 3D distribution before and after simultaneous rotation of polarization vectors proves that experimental data are reliably measured and that the imaging machine works well.

III. RESULTS

A. Reactant preparation

The $O(^1D)$ reactant is produced by 193 nm photodissociation of the N_2O precursor molecule,

$$N_2O(X\ ^1\Sigma^+[1\ ^1A']) + h\nu \rightarrow N_2O(2\ ^1A'[^1\Sigma^+]) \rightarrow N_2 + O(^1D), \quad (2)$$

with an absorption cross section of 8×10^{-20} cm^2 mol^{-1} at 148 K[42,43] and a $O(^1D)$ quantum yield larger than 0.95.[44–49] The most probable translational energy of $O(^1D)$ fragments is approximately 1.2 eV corresponding to a speed of 3800 m/s. The maximum translational energy is 1.8 eV (4670 m/s).[45,50–55] The bond angle corresponding to 193 nm excitation was calculated to be 160°.[56] Thus, those N_2O molecules that have this geometry at the time of photon absorption will preferentially be dissociated. The anisotropy parameter β, which describes the angular distribution $P_N(\alpha)$ of the $O(^1D)$ fragments with respect to the electric field vector of the dissociation laser according to

$$P_N(\alpha) \sim \sin\alpha[1+\beta P_2(\cos\alpha)] \quad (3)$$

depends on the rotational state of the N_2 partner fragment and is 0.96 for $N_2(J=66)$ and 0.44 for $N_2(J=78)$.[53] Here, α is the angle of the $O(^1D)$ momentum vector with the electric field vector of the dissociation laser, P_2 is the second Legendre polynomial. Accordingly, the momentum vector of the $O(^1D)$ fragment forms an angle ρ of 77.4° with the transition dipole moment μ for $N_2(J=66)$ and of 46.1° for $N_2(J=78)$.[57] In *ab initio* calculations it was shown that the transition dipole moment for the $2\ ^1A'-1\ ^1A'$ transition is oriented along the NO bond with a deviation of a few degrees only. Thus, the complementing angles $\pi-\rho$ essentially correspond to the bond angle of the dissociating N_2O molecule, in very good

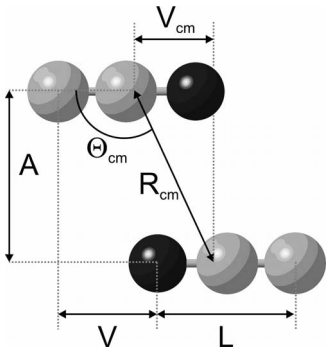

FIG. 1. Equilibrium geometry of the most stable, nonpolar antiparallel slipped $(N_2O)_2$ dimer configuration. Experimental and theoretical parameters are listed in Table I.

agreement with the properties of the potential energy surfaces.

The dimer $(N_2O)_2$ as the smallest possible N_2O van der Waals complex is readily formed in three-body collisions in a supersonic jet expansion,

$$N_2O + N_2O + M \rightarrow (N_2O)_2^* + M \rightarrow (N_2O)_2 + M^*. \quad (4)$$

The dimer formation probability is therefore coupled to the three body collision probability, which for the pure gas quadratically depends on the total stagnation pressure p_0 and linearly on the orifice diameter D. For seeded beams of a few percent N_2O in argon or helium as employed in this work the three body collision probability depends quadratically on the N_2O partial pressure while the carrier gas is present in excess. Conditions can be chosen such that the dimer is the most abundant complex size.[58] The dimer configuration has thoroughly been studied experimentally and theoretically.[59–65] In the most stable geometry the two N_2O molecules form a nonpolar dimer with the two N_2O molecules aligned antiparallel to each other with the oxygen atoms pointing to the inner side of the complex, as shown in Fig. 1. The corresponding structural parameters are listed in Table I. A recently observed polar isomer is thought to be less stable and is much less likely to lead to a reaction after dissociation of one of its constituents, which is why it will not be considered in the analysis section.[65]

Preparation of the $(N_2O)_2$ dimer and initiation of reaction (1) in the dimer is evidenced by several facts. A threshold behavior is observed for the onset of the signal. With nozzle stagnation pressures below 2 bar, no signal can be detected at mass 30 (NO). For stagnation pressures of 2 bars and above, a quadratic dependence of the signal on the stagnation pressure is observed. For a bulk reaction the signal intensity should gradually go to zero, and a correspondingly (small) signal should be observable for pressures below 2 bar. To further investigate this effect we have reduced the distance between the nozzle and the detection volume by a factor of 5, thereby increasing the density by a factor of 25. Again, the threshold was found at a stagnation pressure of 2 bar, which is conceivable only if a van der Waals complex is responsible for generating the signal.

Unfortunately, under our experimental conditions a direct mass spectroscopic detection of this complex is not possible since it undergoes fragmentation to monomers or their fragments prior to detection.[66] Alternatively, the nature of the complex can be investigated by changing the expansion conditions. Experiments were performed at varied stagnation pressures for the neat sample and for seeded beams of different concentrations in helium and in argon carrier gas. The threshold value and the shape of the signal were found to be independent of these variations. Therefore we conclude that the species responsible for generating our signal must be the same in all experimental runs, with the only species common to all experiments performed being $(N_2O)_n$ van der Waals complexes. If the stagnation pressure is now chosen to be close to the threshold for signal appearance, then experimental conditions are similar to those of Miller *et al.*[58] who reported a prevailing production of dimers compared to higher order complexes.

Last, our experimental observations of a cold rotational distribution for all observed vibrational levels and a monotonically decreasing vibrational distribution are in very good agreement with the observations of Honma *et al.*[25] who initiated reaction (1) in the dimer, but contradict to the experimental findings for the bulk initiated reaction.[14–16] Therefore, the reaction products monitored in the measurements presented in this work must essentially have been produced by photoinitiating reaction (1) in the $(N_2O)_2$ dimer.

B. Product quantum state population

In Figs. 2 and 3 rotationally resolved spectra of several vibrational bands of the $A\ ^2\Sigma^+ - X\ ^2\Pi_\Omega$ electronic transitions for nascent NO are presented. The spectra were obtained by plotting the integrated ion signal over the wavelength. All lines were observed only for larger stagnation pressures than 2 bar, with both dissociation and analyzing laser operating and carefully brought to spatial and temporal overlap. Line positions were calculated with the LIFBASE (V2.0.55) software.[67]

Figure 2 shows the experimental and simulated spectra for the $A\ ^2\Sigma^+(v'=0,J') - X\ ^2\Pi_\Omega(v''=0,J'')$ transition together with the assignment of individual lines and rotational branches.

TABLE I. Structural parameters of the most stable, nonpolar antiparallel slipped $(N_2O)_2$ dimer configuration. Experimental data are taken from Ref. 65. Theoretical values were calculated with the Gaussian program package using MP2 perturbation theory with the aug-cc-pVTZ basis set (Ref. 66). Parameters are defined in Fig. 1. Distances are given in picometers.

	Θ_{cm}	R_{cm}	A	V_{cm}	V	L
Theoretical values	119.6°	336.3	292.4	166.1	169.3	233.7
Experimental values	119°	342.3	299.4	165.9		

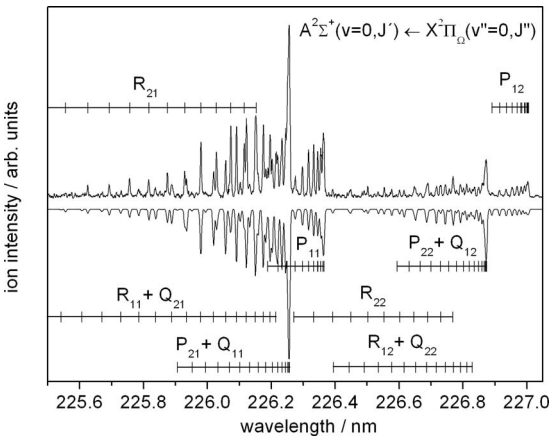

FIG. 2. Experimental and simulated spectra for the $A\ ^2\Sigma^+(v'=0,J')-X\ ^2\Pi_\Omega(v''=0,J'')$ transition and assignment of individual lines and rotational branches. Upper trace: experimental spectrum. Lower trace: simulated spectrum for $T=150$ K.

The rotational temperature T_R was determined from integrated line intensities. As can be seen from Fig. 2, a sufficient number of nonoverlapping lines exist only for P_{12} and R_{21} branches. Taking into account the Hönl–London factors for these two branches[68,69] we calculated temperatures of $T_R(P_{12})=(147\pm28)$K and $T_R(R_{21})=(133\pm10)$K, respectively, resulting in a mean value of $T_R=137$ K. This value is an additional proof that the observed NO was produced in reaction (1) and was not initially present in the vacuum chamber as thermal background or in the sample as impurity. In the first case the rotational temperature should approximately be 300 K, in the latter 6 K.

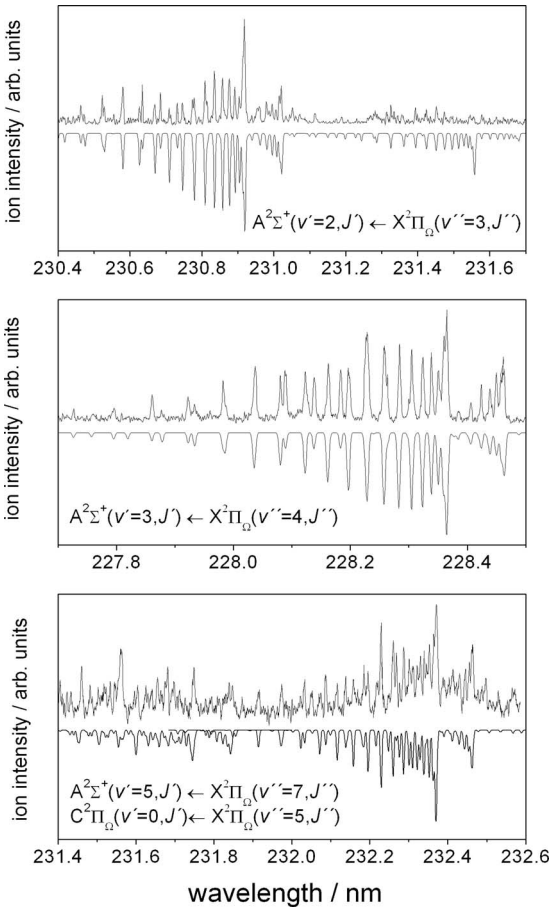

FIG. 3. Experimental and simulated spectra for three vibrational (v',v'') bands of the $A\ ^2\Sigma^+-X\ ^2\Pi_\Omega$ transition: (2,3) (upper panel), (3,4) (middle panel), and (5,7) (lower panel). For short wavelengths, the (5,7) band is accompanied by a minor contribution of the $C\ ^2\Pi_\Omega(v'=0)-X\ ^2\Pi_\Omega(v''=5)$ transition. Upper traces: experimental spectra. Lower traces: simulated spectra for $T=150$ K. All spectra are equally well described by the same rotational temperature of 150 K.

In the top panel of Fig. 3, the rotationally resolved vibrational band of the $A\ ^2\Sigma^+(v'=2,J')-X\ ^2\Pi_\Omega(v''=3,J'')$ transition is presented together with a simulated spectrum assuming a rotational temperature of 150 K. Only a qualitative analysis of the relative integrated intensities for different vibrational bands can be performed because several experimental parameters (laser intensity, stagnation pressure, laser-valve delay time, etc.) had to be optimized for monitoring the spectra.

The signal intensity is affected by the population of the lower vibrational state of a given transition and by the corresponding Franck–Condon factor. Experimentally, the best qualitative criterion for the signal intensity is the signal to noise ratio. Taking into account the well-known Franck–Condon factors for the different vibrational bands,[70] one can induce qualitative information on the relative populations of the lower vibrational states.

The Franck–Condon factors $q_{v'v''}$ for the transition from the $X(v''=0)$ state to the $A(v'=0)$ state and for the transition from the $X(v''=3)$ state to the $A(v'=2)$ state are of the same order of magnitude ($q_{00}=1.7\times10^{-1}$ and $q_{23}=7.4\times10^{-2}$),[70] but signal to noise for the (0,0) transition is much larger than for the (2,3) transition. Therefore, the population of the $X(v''=3)$ state is considerably smaller than that of the $X(v''=0)$ state. The rotational temperature, however, is virtually unchanged as is demonstrated by the very good agreement between the 150 K simulation and the experimental spectrum in the top panel of Fig. 3.

The spectra of the $A\ ^2\Sigma^+(v'=3,J')-X\ ^2\Pi_\Omega(v''=4,J'')$ and the $A\ ^2\Sigma^+(v'=5,J')-X\ ^2\Pi_\Omega(v''=7,J'')$ transitions shown in the middle and the lower panels of Fig. 3 allow to draw similar conclusions. The signal to noise ratio reflects the slightly smaller Franck–Condon factors $q_{34}=1.1\times10^{-1}$ and $q_{57}=6.6\times10^{-2}$ together with a significantly smaller population of the corresponding lower vibrational levels.[70] Again, the rotational temperature appears to be essentially unchanged, and both bands can very well be simulated using a rotational temperature of 150 K.

All spectra shown in Figs. 2 and 3 result from $A\ ^2\Sigma^+-X\ ^2\Pi_\Omega$ excitation. Attempts to employ the $D(^2\Sigma^+)$ state as resonant intermediate state in the ionization of NO were unsuccessful. Only at the high energy side of the $A\ ^2\Sigma^+(v'=5)-X\ ^2\Pi_\Omega(v''=7)$ band some weak lines could be observed that result from the $C\ ^2\Pi_\Omega(v'=0)-X\ ^2\Pi_\Omega(v''=5)$ transition. While the small signal to noise ratio does not allow a quantitative analysis of signal intensities, the good agreement between experimentally observed and simulated line positions prove the existence of nascent NO reaction products in the $X\ ^2\Pi_\Omega(v''=5)$ state.

C. 3D product momentum distributions

3D velocity map imaging allows the complete determination of the momentum vector for each detected particle. Since ionization has a negligible effect on the particle momentum, the measured momentum is a result of the forces acting during the bimolecular reaction in which the particle was generated. "Complete determination" in this context means the simultaneous measurement of all three momentum components. Since the ionization occurs quantum state selectively via a resonant intermediate state, in addition to the full 3D momentum vector the quantum state of the particle is also known. Thus, by selecting an appropriate detection laser wavelength a quantum state specific 3D momentum vector distribution for every rovibronic quantum state is obtained upon collection of sufficiently many individual events.

This quantum state specific 3D momentum vector distribution contains the complete information about the product formed in the bimolecular reaction. In particular, suitable projection procedures allow to obtain quantities commonly referred to in the investigation of reaction dynamics, e.g., the one-dimensional speed distribution $P(v)$, the speed-dependent anisotropy parameter $\beta(\mathrm{v})$, and the like. Note, that the 3D distribution always contains the complete information. Hence, every quantity obtained by some projection of the 3D distribution did not require any mathematical reconstruction and contains less information than the original distribution due to the projection procedure. For details the reader is referred to Ref. 1.

For the NO products observed in this work, no significant differences between different rotational transitions of the same vibrational bands were expected due to the very small energy differences associated with different NO rotational quantum states. This expectation was verified for a set of selected rovibrational transitions. As a consequence, for the data analysis presented below, only the strongest rovibrational transition of each vibrational band was thoroughly analyzed in detail. Results obtained in this way are characteristic for all members of a vibrational band.

Any 2D image of a 3D distribution requires a certain projection as well. The chosen projection procedure can in principle arbitrarily be defined. Here, for reasons outlined in Refs. 1 and 10 the so-called meridian projection was chosen for generating the images shown in Figs. 4 and 5.

In meridian projection a projection plane is chosen by the definition of a spherical coordinate system. The end point of each individual single particle momentum vector $\vec{p_i}=(R_i,\vartheta_i,\varphi_i)$ is projected onto the corresponding meridian by replacing the polar angle ϑ_i by the value $\pi/2$ while azimuth angle φ_i and radius R_i remain unchanged, $\vec{p_i}=(R_i,\vartheta_i,\varphi_i)\rightarrow\vec{p_i^M}=(R_i,\pi/2,\varphi_i)$. Depending on the orientation of the spherical coordinate system there are three such meridian projections which use the xy, xz, and yz plane as plane of projection, respectively. The three projections together contain the same information as the original 3D distribution whereas the information loss in the polar angle coordinate associated with the projection procedure is obvious. Note that here 2D images are constructed from the measured 3D distribution under loss of information while the standard imaging analysis relies on the reconstruction of the 3D distribution from measured 2D projections under the assumption of certain symmetry properties.

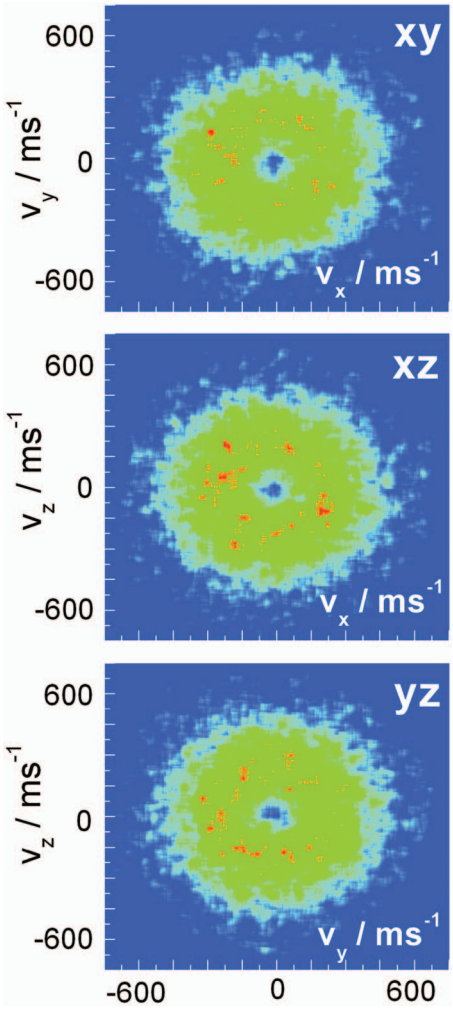

FIG. 4. The three possible meridian projections for the $A\,^2\Sigma^+(v'=3,J')-X\,^2\Pi_\Omega(v''=4,J'')$ transition. All three projections are nearly identical to each other.

Figure 4 shows all three possible meridian projections for the $A\,^2\Sigma^+(v'=3,J')-X\,^2\Pi_\Omega(v''=4,J'')$ transition. All three projections are nearly identical to each other. The 2D distributions are radially symmetric, with a single maximum at a relatively small speed of ca. 300 m/s. Identical distributions for all three projections are evidence of an almost isotropic momentum distribution. The same behavior is observed for the (0,0) and (5,7) transitions, which are not shown in detail.

Figure 5 shows the xy meridian projection for the vibrational bands (0,0), (3,4), and (5,7). Again, apart from a variation in the signal to noise level the projections are nearly identical to each other for all three vibrational bands. This unexpected and surprising result will in detail be discussed in Sec. IV.

IV. DISCUSSION

A. Densities and number distributions

Traditionally, normalized angular distributions are expressed as densities.[71] If angular distributions are to be de-

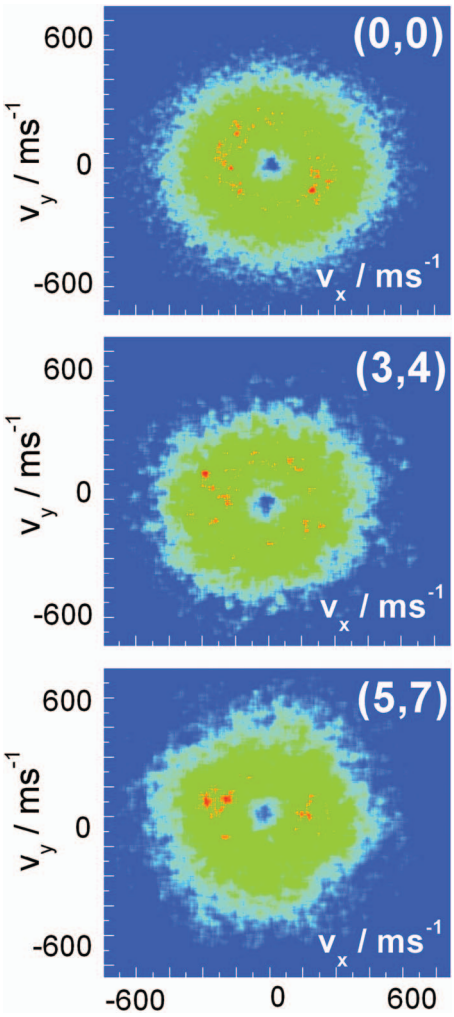

FIG. 5. *xy* meridian projections for the vibrational bands (0,0), (3,4), and (5,7) of the $A\ ^2\Sigma^+ - X\ ^2\Pi_\Omega$ transition. The projections are nearly identical to each other for all three vibrational bands.

termined from experimental data involving integration over one or more variables, it is more convenient to express angular distributions in terms of number distributions than in terms of densities, the reason being that the division by small numbers for very slow particles ($v \to 0$) or in the vicinity of the pole ($\vartheta \to 0$) can be avoided in data analysis.

In order to avoid confusion with respect to the actual nature of the distributions dealt with later on in this work, below we discuss the differences between densities P_D and number distributions P_N. A velocity vector density $P_D(v, \vartheta, \varphi)$ e.g., specifies the density of particles with a velocity vector end point for a given point (v, ϑ, φ) in 3D space and is normalized by

$$\int\int\int v^2 \sin\vartheta dv d\vartheta d\varphi \{P_D(v,\vartheta,\varphi)\} = 1. \tag{5}$$

The velocity vector distribution $P_N(v, \vartheta, \varphi)$ specifies the actual number of particles with a velocity vector end point for a given point (v, ϑ, φ) in 3D space. Accordingly, $P_N(v, \vartheta, \varphi)$ is normalized by

$$\int\int\int dv d\vartheta d\varphi \{P_N(v,\vartheta,\varphi)\} = 1. \tag{6}$$

Consequently, the velocity vector density $P_D(v, \vartheta, \varphi)$ and the velocity vector distribution $P_N(v, \vartheta, \varphi)$ are related to each other by

$$P_N(v,\vartheta,\varphi) = v^2 \sin\vartheta P_D(v,\vartheta,\varphi). \tag{7}$$

The same holds for any projections. For example, the speed dependent angular density $P_D(v, \vartheta)$ and the speed density $P_D(v)$ are obtained from the 3D velocity vector density $P_D(v, \vartheta, \varphi)$ by performing the integrations

$$P_D(v,\vartheta) = \int d\varphi \{P_D(v,\vartheta,\varphi)\}, \tag{8a}$$

$$P_D(\mathrm{v}) = \int\int \sin\vartheta d\vartheta d\varphi \{P_D(v,\vartheta,\varphi)\}, \tag{8b}$$

and the speed dependent angular distribution $P_N(v, \vartheta)$ and the speed distribution $P_N(v)$ are obtained from the 3D velocity vector distribution $P_N(v, \vartheta, \varphi)$ by performing the integrations,

$$P_N(v,\vartheta) = \int d\varphi \{P_N(v,\vartheta,\varphi)\}, \tag{9a}$$

$$P_N(v) = \int\int d\vartheta d\varphi \{P_N(v,\vartheta,\varphi)\}. \tag{9b}$$

Thus, densities and distributions are related to each other by

$$P_N(v,\vartheta) = v^2 \sin\vartheta P_D(v,\vartheta), \tag{10a}$$

$$P_N(v) = v^2 P_D(v). \tag{10b}$$

If not otherwise stated, throughout this work we will use distributions P_N instead of densities P_D. Note that for the speed dependent angular distribution v is not a variable, so the scaling factor between angular density and angular distribution is given by $\sin\vartheta$, and v^2 plays the role of a normalization constant only.

B. Product anisotropy and polarization effects

Generally, a bimolecular reaction involving one aligned reactant and a polarized detection laser, like the reaction studied in this work, can give rise to product alignment or orientation, which can in extension of Eq. (3) be described by an expansion to a series of Legendre polynomials including higher orders. In view of the apparent spatial product isotropy visible in Figs. 4 and 5, the analysis of the angular dependence of the product density can be limited to employing Eq. (3) to investigate to what degree the anisotropy of the $O(^1D)$ precursor is carried on the observed NO reaction product. The speed-dependent β parameter is obtained by fitting the angular distribution $P_N(\alpha)$ [Eq. (3)] to the azimuth angle integrated 3D distribution: $\int d\varphi(P_N(v,\alpha,\varphi))$ for a given value of v. The results of this analysis are shown in Fig. 6

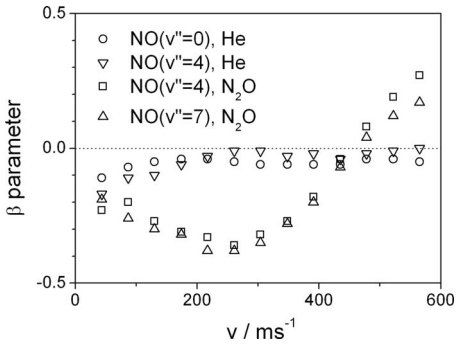

FIG. 6. Speed dependent anisotropy parameters $\beta(v'')$ for different vibrational states [circles: NO($v''=0$), expansion in light carrier gas; downward triangles: NO($v''=4$), expansion in light carrier gas; squares: NO($v''=4$), neat gas expansion; upward triangles: NO($v''=7$), neat gas expansion]. For light carrier gases isotropic product distributions are correctly observed, independent of the vibrational state. For the neat gas expansion artifacts from background gas contributions are introduced, which cannot be removed from the data. However, the similarity of the distorted anisotropy behavior observed for NO($v''=4$) and for NO($v''=7$) suggests that the reaction process itself is essentially isotropic for NO($v''=7$) as well.

When helium is used as a carrier gas the β parameter vanishes for all speeds v, independent of the NO vibrational level, as anticipated from the data shown in Figs. 4 and 5. However, when neat N_2O is expanded, the behavior is different. This is clearly an experimental artifact, as becomes clear from NO($v''=4$) for which both behaviors can be observed depending on the choice of the carrier gas. It can be explained by contributions from background that cannot be removed and affect the determination of β when neat beams of reactants are used. For high vibrational states as NO($v''=7$) where only neat beams of reactants provided enough signal for products to be detected, this artifact could not be removed from the measured data. However, the similar behavior of NO($v''=4$) and NO($v''=7$) when expended in a neat beam let us conclude that also for NO($v''=7$) no pronounced anisotropy is induced in the reaction itself.

The rotation of only the polarization vector of the analyzing laser with respect to the polarization vector of the dissociation laser will result in different 3D distributions if alignment effects are important. The failure to observe any such changes proves that alignment effects are absent or too small to be detectable with our experimental sensitivity.

C. Speed distributions

Speed distributions were calculated according to Eq. (9b) for the vibrational states $v''=0$, $v''=4$, and $v''=7$. They are obtained by angular integration of the meridian projections. In Fig. 7, the speed distribution belonging to the top panel ($v''=0$) of Fig. 5 is displayed. The speed distribution is singly peaked, with a maximum occurring at 290 m/s and a low amplitude tail well extending to speeds up to 2500 m/s. The shape of the speed distribution is essentially independent of the quantum state of the observed NO product as is suggested by the meridian projections shown in Fig. 5.

If the intensity of the dissociation laser is increased, a nonresonant NO signal starts to appear, which has a significantly different speed distribution. The additional signal persists if the dye laser is switched off. Therefore this signal must be due to a process induced by 193 nm radiation exclusively. Only the amplitude of the speed distribution associated with the nonresonant signal is intensity dependent, not its shape. Thus, any explanation employing space charge arguments due to a large ion density in the focal volume cannot explain the observed effect. The speed distribution associated with the nonresonant signal is shown in Fig. 8.

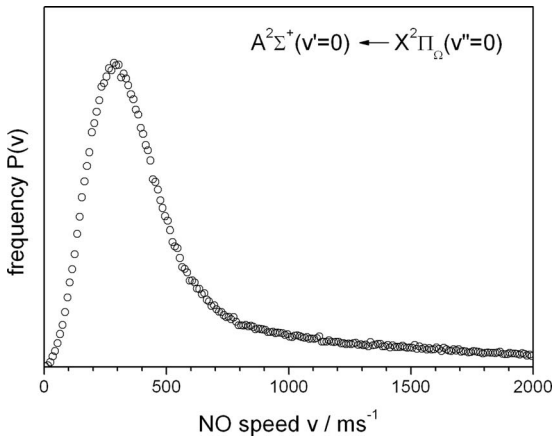

FIG. 7. MB frame speed distribution obtained for resonant detection of NO($X\ ^2\Pi_\Omega, v''=0$).

The nonresonant speed distribution consists of two maxima. One is essentially identical to the observed resonant speed distributions. The second maximum occurs at larger speeds and is centered near 1700 m/s, extending well up to 2800 m/s.

Since NO has a relatively low ionization potential of 9.2639 eV, above an internal excitation of 2.83 eV one-photon ionization of NO by 193 nm radiation becomes energetically possible. This excitation energy corresponds to $v''>13$.[70] We believe that the nonresonant distribution of Fig. 8 is significantly contributed to by highly vibrationally excited NO products with vibrational excitation with $v''>13$. This interpretation agrees very well with the product velocity and angular scattering distributions for products formed in $v''=16$ and 17 reported for the nonconstrained gas-phase reaction.[19] Implications of this observation will in detail be discussed in Sec. IV D.

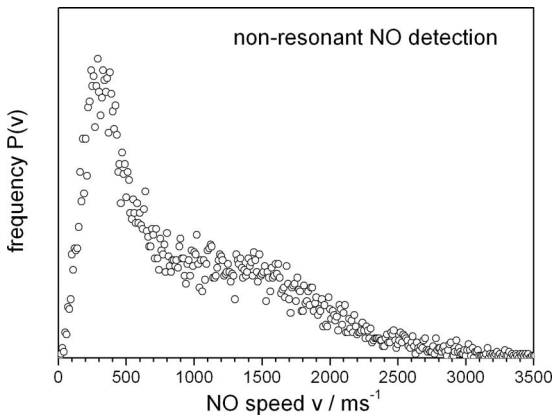

FIG. 8. MB frame speed distribution obtained with the dissociation laser alone. The low speed peak resembles the resonantly observed distribution of Fig. 7 and is due to an accidental resonance of the 193 nm dissociation laser with $D(^2\Sigma^+, v'=1)-X(^2\Pi, v''=2)$ transition. The high speed peak results from one-photon ionization of highly vibrationally exited NO($v''\geq 13$).

Direct production of NO from photodissociation of N_2O at 193 nm as alternative explanations can be ruled out. Although the photodissociation of N_2O at 193 nm,

$$N_2O + 193\ \text{nm} \rightarrow N(^4S) + NO, \tag{11}$$

is energetically possible, several arguments prove that this reaction cannot be the origin of the observed nonresonant signal. First, the quantum yield for this spin-forbidden process was found to be negligibly small.[47,48] Second, its dissociation energy is 4.92 eV, resulting in an available energy of 1.47 eV at a dissociation wavelength of 193 nm. The corresponding maximum speed for the NO fragment is 1740 m/s, significantly smaller than the observed maximum speed. Third, the available energy of 1.47 eV would allow to only populate the vibrational levels 0 to 5 of the NO molecule. Therefore the high speed NO fragments should also be observed by the resonant detection scheme of Figs. 1 and 2.

D. Energy partitioning

For the analysis of the energy partitioning it is necessary to distinguish between two reference systems, the first being the MB frame and the second being the center of mass frame (CM) of the $O(^1D)+N_2O$ reaction system. The latter is of course identical to the CM frame of the $NO(s)+NO(f)$ products. Letters in parentheses (s: Slow, f: Fast) are given to distinguish between the two chemically identical NO molecules generated in the same elementary process, one containing the newly formed bond and the other containing the NO bond already existent in the N_2O molecule. They possess different kinetic energies as will be outlined below. All speed distributions shown in this work are referenced to the MB system. Just for the sake of completeness it should be mentioned that in principle a third reference system exists, which is the laboratory frame. Although it might seem to be the most natural reference frame for the performed measurements, it is not suitable and never used for the analysis of the experimental results and hence will not be discussed further.

Let us first consider the CM energies of the reaction system on the basis of thermochemical data and the energy partitioning in the N_2O photodissociation. The CM available energy in reaction (1) is given by the sum of the reaction enthalpy $\Delta_R H$, the CM collision energy E_{coll}, and the internal energy E_{int} of the reactants. The latter is taken to be 0 because N_2O is efficiently cooled in the MB. The CM collision energy amounts to $m(N_2O)/[m(N_2O)+m(O)]=44/60$ (73.3%) of the MB kinetic energy of the $O(^1D)$ atom with the remaining $m(O)/[m(N_2O)+m(O)]=16/60$ (26.7%) appearing as MB kinetic energy of the CM of the reaction system. The most probable MB kinetic energy of $O(^1D)$ produced by 193 nm photolysis of N_2O is 1.2 eV,[52] corresponding to a most probable CM collision energy of 0.88 eV and a most probable MB kinetic energy of the CM of 0.32 eV. With a 0 K reaction enthalpy of 3.55 eV for reaction (1) (Ref. 72) the most probable value for the CM available energy to be distributed between the two NO products is calculated to be 4.43 eV.

Now consider a $NO(s)$ product the MB speed distribution of which is shown in Fig. 7 for the case $v''=0$ and which peaks at a MB speed of 290 m/s. The most probable MB kinetic energy of the CM of 0.32 eV corresponds to a MB speed of the CM of 1015 m/s. The CM speed of the $NO(s)$ product is given by the difference of its MB speed and the MB speed of the CM. The most probable CM speed of the $NO(s)$ product in $v''=0$ is therefore calculated to be −725 m/s, the negative sign indicating a backward scattering of the $NO(s)$ product with respect to the movement of the CM. Since by definition the momenta of both $NO(s)$ and $NO(f)$ products in the CM frame must cancel each other, the most probable CM speed of the $NO(f)$ partner product must be +725 m/s, resulting in a most probable MB speed of the $NO(f)$ partner product of 1740 m/s. All values are summarized in Table II. Although NO products with MB speeds of 1740 m/s have been observed in our experiments employing resonant detection of NO by (1+1)-REMPI, they are by far outnumbered by much slower products with speeds around the most probable MB speed of 290 m/s. This imbalance indicates that we have not been able to observe all NO products generated in reaction (1) with the same sensitivity. Note however, that the nonresonant MB speed distribution shown in Fig. 8 does exhibit a second maximum exactly centered at the calculated value of 1740 m/s.

TABLE II. Most frequent kinetic energies E_{kin} and speeds v of the reactants of the reaction $O(^1D)+N_2O \rightarrow NO(s)+NO(f)$ in MB and CM frames. Energies are given in eV, speeds in m/s. The experimentally determined MB values for $NO(s)$ are given in italics. They refer to NO in its vibrational ground state (cf. Fig. 7).

	Reference frame			
	MB (E_{kin}/eV)	CM (E_{kin}/eV)	MB [v/(m/s)]	CM [v/(m/s)]
$O(^1D)$	1.2	0.65	3800	2785
N_2O	0	0.23	0	1015
CM $[O(^1D)+N_2O]$	0.32	0	1015	0
$NO(s)$	*0.01*	0.08	*290*	−725
$NO(f)$	0.47	0.08	1740	725

The imbalance mentioned in the preceding paragraph becomes even more pronounced when the total energy balance is considered. The most probable CM speed of 725 m/s corresponds to a most probable CM kinetic energy of only 80 meV per NO product, or to a total CM kinetic energy of 0.16 eV. This value for the most probable total CM kinetic energy leaves the very large amount of 4.43−0.16 eV=4.27 eV, which must appear as total internal energy of both products $NO(s)+NO(f)$. Considering the low rotational temperature of the resonantly observed NO products of only 150 K and the decreasing population for increasing vibrational quantum numbers, it is evident that NO products with very large internal energy must be generated in reaction (1), which escape observation by our (1+1)-REMPI detection scheme. In particular, $NO(s)$ products in $v''=0$, which are the most abundant products observed in our experiment should have $NO(f)$ partner products with internal energies of more than 4 eV. Whether this internal energy occurs as rotation or vibration cannot directly be determined from our experimental results.

In this context, the nonresonant MB speed distribution presented in Fig. 8 deserves special attention. The low en-

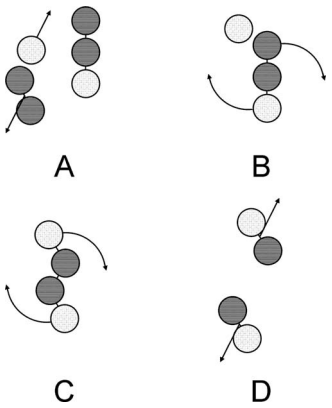

FIG. 9. Visualization of the dimer rearrangement (a). After absorption of the 193 nm photon, $O(^1D)$ moves at a small angle to the axis of the N_2O molecule. (b) $O(^1D)$ hits the N_2O molecule, which starts to rotate. (c) The O–N–N–O complex takes on its trans-shaped minimum (Ref. 32). (d) Finally, NO products fly along the initial velocity vector of $O(^1D)$.

ergy peak has a maximum at the same speeds as the resonantly observed distributions. It is due to the accidental resonance of the 193 nm radiation of the dissociation laser with the $D(^2\Sigma^+, v'=1)-X(^2\Pi, v''=2)$ transition in NO. Since the MB speed distribution of the $X(^2\Pi, v''=2)$ state of NO(*s*) is known to be singly peaked at low MB speeds, the high MB speed peak in Fig. 8 must be due to another ionization process. Single photon ionization of highly internally excited NO with 193 nm photons becomes possible for vibrational excitation of $v'' \geq 13$, which is why we believe that the high energy peak of the nonresonantly observed MB speed distribution of Fig. 8 results from this process. Unfortunately, no REMPI excitation scheme exists for these highly vibrationally excited levels, so that the only experimental evidence for the existence of such highly excited NO(*f*) products is the speed distribution shown in Fig. 8.

E. Mechanism

From the observed 3D distribution, the extracted spatial and speed distributions, we have clearly identified the existence of NO products with very different physical properties. NO(*s*) products accessible to resonant detection by (1+1)-REMPI are generated with low vibrational, rotational, and translational excitation, and are preferentially backward scattered with respect to the direction of motion of the CM of the reaction system, i.e., also with respect to the direction of motion of the $O(^1D)$ photofragment fragment. The corresponding NO(*f*) product must consequently be forward scattered and contain very large internal energies of up to 4 eV and more, which is most likely released as vibrational excitation. A portion of these NO(*f*) products was observed by nonresonant one-photon ionization with 193 nm light.

A simplified visualization of the proposed mechanism is shown in Fig. 9. The slipped antiparallel geometry of the $(N_2O)_2$ dimer restricts the angle of attack of the $O(^1D)$ atom with respect to the N_2O internuclear axis to small values [Fig. 9(a)]. Conservation of angular momentum requires the resulting O–N–N–O moiety to rotate [Fig. 9(b)]. At the same time it will try to reach its minimum energy transconformation [Fig. 9(c)].[32] The torque resulting from N–N bond fission will compensate the oppositely directed torque resulting from $O(^1D)$ impact on the N_2O molecule and the two NO products will be formed rotationally cold [Fig. 9(d)]. Moreover, abstraction of the terminal N by $O(^1D)$ will leave the "old" NO in a spectator role with only little vibrational energy transfer whereas the "new" NO should be formed with a significant amount of vibrational energy. Since the direction of motion of $O(^1D)$ and the breaking N–N bond are oriented essentially parallel to each other, the abstraction process will result in a pronounced forward scattering of the newly formed, highly vibrationally excited NO. Its counterpart, the old NO in the spectator role, will remain rotationally and vibrationally cold and consequently undergo backward scattering.

We are led to identify the old backward scattered and internally cold NO with those slow products that have resonantly been observed by (1+1)-REMPI excitation, whereas the corresponding fast, forward scattered, internally hot NO products could only be observed by nonresonant 193 nm one-photon ionization. The proposed mechanism must be regarded to be a consequence of the restricted slipped antiparallel geometry of the $(N_2O)_2$ dimer. The part of the potential energy surface sampled by the incoming $O(^1D)$ atom is a strongly restricted subset of the potential energy surface available to $O(^1D)$ atoms produced under bulk conditions. Trajectory calculations on the $O(^1D)+N_2O$ potential energy surface accounting for the geometrical restriction of the dimer configuration should help to corroborate the suggested mechanism.

V. CONCLUSION

The reaction $O(^1D)+N_2O \rightarrow NO+NO$ has been initiated in a $(N_2O)_2$ van der Waals complex. NO products have been state-selectively analyzed by the 3D velocity map imaging technique. The dimer was produced by a supersonic MB expansion. Product properties are strikingly different from products generated in the bulk reaction. Previous results on vibrational and rotational excitation were confirmed.[25]

- Vibrational excitation of NO was detected from $v''=0$ to $v''=7$. Higher vibrational states are less populated than lower ones. Vibrational states with $v''>7$ are likely to be populated, but are not detectable by the employed (1+1)-REMPI scheme.
- Rotational excitation in all studied vibrational bands is very low and can well be described by a rotational temperature of ca. 150 K.
- Translational excitation has been determined for the first time. In the MB frame products are very slow, i.e., the speed of NO in the $O(^1D)+N_2O$ CM frame must be of similar absolute value, but of opposite sign than the speed of the CM in the MB frame. In other words, all observed NO products are pronouncedly backward scattered.
- The spatial distribution of the backward scattered products has been determined with unprecedented accuracy. In the MB frame it was found to be isotropic. Ironically,

the observed isotropy is evidence of a highly anisotropic reactive collision.

- Nonresonantly ionized NO products were observed with kinetic energies matching the forward scattered partners of the resonantly ionized, backward scattered products. The lack of resonant detection proves these products must be generated in $v>7$.
- Forward scattered NO products must carry very large rovibrational excitation in the order of 4 eV.

The pronounced difference between products generated from the bulk reaction and from the reaction initiated in the dimer is due to a restrained reaction geometry, which allows to sample only a small part of the potential energy surface controlling the $O(^1D)+N_2O$ system.

ACKNOWLEDGMENTS

This work was performed in collaboration with the Braunschweig International Graduate School of Metrology (IGSM). Financial support of the Deutsche Forschungsgemeinschaft and the Alexander von Humboldt Foundation is gratefully acknowledged.

[1] S. Kauczok, N. Gödecke, A. I. Chichinin, C. Maul, and K.-H. Gericke, "3D Velocity Map Imaging: Set-up and resolution improvement compared to 3D ion imaging," Rev. Sci. Instrum. (submitted).
[2] T. S. Einfeld, A. I. Chichinin, C. Maul, and K.-H. Gericke, J. Chem. Phys. **116**, 2803 (2002).
[3] T. S. Einfeld, A. I. Chichinin, C. Maul, and K.-H. Gericke, J. Chem. Phys. **117**, 1123 (2002).
[4] T. S. Einfeld, A. I. Chichinin, C. Maul, and K.-H. Gericke, J. Chem. Phys. **117**, 4214 (2002).
[5] L. Schäfer, N. Gödecke, O. Ott, C. Maul, K.-H. Gericke, P. S. Shternin, E. V. Orlenko, and O. S. Vasyutinskii, Chem. Phys. **301**, 213 (2004).
[6] A. I. Chichinin, T. S. Einfeld, C. Maul, and K.-H. Gericke, Chem. Phys. Lett. **390**, 50 (2004).
[7] A. I. Chichinin, T. S. Einfeld, K.-H. Gericke, J. Grunenberg, C. Maul, and L. Schäfer, Phys. Chem. Chem. Phys. **7**, 301 (2005).
[8] A. I. Chichinin, T. S. Einfeld, C. Maul, and K.-H. Gericke, Dokl. Phys. Chem. **402**, 96 (2005).
[9] A. I. Chichinin, T. S. Einfeld, C. Maul, and K.-H. Gericke, Dokl. Phys. Chem. **407**, 72 (2006).
[10] A. I. Chichinin, C. Maul, and K.-H. Gericke, J. Chem. Phys. **124**, 224324 (2006).
[11] A. I. Chichinin, P. S. Shternin, N. Gödecke, S. Kauczok, C. Maul, O. S. Vasyutinskii, and K.-H. Gericke, J. Chem. Phys. **125**, 034310 (2006).
[12] G. P. Brasseur, J. J. Orlando, and G. S. Tyndall, *Atmospheric Chemistry and Global Change* (Oxford University Press, New York, 1999).
[13] N. Goldstein, G. D. Greenblatt, and D. R. Wiesenfeld, Chem. Phys. Lett. **83**, 21 (1983).
[14] X. B. Wang, H. Z. Li, Q. H. Zhu, F. N. Kong, and H. G. Yu, J. Chin. Chem. Soc. (Taipei) **42**, 399 (1995).
[15] H. Akagi, Y. Fujimura, and O. Kajimoto, J. Chem. Phys. **111**, 115 (1999).
[16] G. Hancock and V. Haverd, Phys. Chem. Chem. Phys. **5**, 2369 (2003).
[17] F. Green, G. Hancock, A. J. Orr-Ewing, M. Brouard, S. P. Duxon, P. A. Enriquez, R. Sayos, and J. P. Simons, Chem. Phys. Lett. **182**, 568 (1991).
[18] M. Brouard, S. P. Duxon, P. A. Enriquez, R. Sayos, and J. P. Simons, J. Phys. Chem. **95**, 8169 (1991).
[19] M. Brouard, S. P. Duxon, P. A. Enriquez, and J. P. Simons, J. Chem. Phys. **97**, 7414 (1992).
[20] H. Akagi, Y. Fujimura, and O. Kajimoto, J. Chem. Soc., Faraday Trans. **94**, 1575 (1998).
[21] H. Tsurumaki, Y. Fujimura, and O. Kajimoto, J. Chem. Phys. **111**, 592 (1999).
[22] S. Kawai, Y. Fujimura, O. Kajimoto, and T. Takayanagi, J. Chem. Phys. **120**, 6430 (2004).
[23] P. J. Pisano, M. S. Westley, and P. L. Houston, Chem. Phys. Lett. **318**, 385 (2000).
[24] K. Honma and O. Kajimoto, Chem. Phys. Lett. **117**, 123 (1985).
[25] K. Honma, Y. Fujimura, O. Kajimoto, and G. Inoue, J. Chem. Phys. **88**, 4739 (1988).
[26] I. Last, A. Aguilar, R. Sayós, M. González, and M. Gilibert, J. Phys. Chem. A **101**, 1206 (1997).
[27] M. González, R. Valero, J. M. Anglada, and R. Sayós, J. Chem. Phys. **115**, 7015 (2001).
[28] H. Akagi, A. Yokoyama, Y. Fujimura, and T. Takayanagi, Chem. Phys. Lett. **324**, 423 (2000).
[29] T. Takayanagi and A. Wada, Chem. Phys. **269**, 37 (2001).
[30] T. Takayanagi and H. Akagi, Chem. Phys. Lett. **363**, 298 (2002).
[31] T. Takayanagi, Chem. Phys. **308**, 211 (2005).
[32] S. Kawai, Y. Fujimura, O. Kajimoto, and T. Yamashita, J. Chem. Phys. **124**, 184315 (2006).
[33] Y.-J. Lu, C.-W. Liang, and J. J. Lin, J. Chem. Phys. **125**, 133121 (2006).
[34] S. Kawai, Y. Fujimura, O. Kajimoto, T. Yamashita, C.-B. Li, T. Komatsuzaki, and M. Toda, Phys. Rev. A **75**, 022714 (2007).
[35] A. I. Chichinin, T. S. Einfeld, C. Maul, and K.-H. Gericke, Rev. Sci. Instrum. **73**, 1856 (2002).
[36] A. I. Chichinin, T. S. Einfeld, K.-H. Gericke, and C. Maul, in *Imaging in Molecular Dynamics: Technology and Applications*, edited by B. J. Whitaker (Cambridge University Press, Cambridge, 2003), pp. 138–164.
[37] N. Gödecke, *3D Velocity Mapping: Vollständige Charakterisierung der Bimolekularen Reaktion* $O(^1D)+N_2O\rightarrow NO+NO$ (Cuvillier, Göttingen, 2008).
[38] S. E. Sobottka and M. B. Williams, IEEE Trans. Nucl. Sci. **35**, 348 (1988).
[39] I. Ali, R. Dörner, O. Jagutzki, S. Nüttgens, V. Mergel, L. Spielberger, K. Khayyat, T. Vogt, and H. Bräuning, Nucl. Instrum. Methods Phys. Res. B **149**, 490 (1999).
[40] M. Lampton, O. Siegmund, and R. Raffanti, Rev. Sci. Instrum. **58**, 2298 (1987).
[41] J. Danielak, U. Domin, R. Kępa, M. Rytel, and M. Zachwieja, J. Mol. Spectrosc. **181**, 394 (1997).
[42] G. S. Selwyn and H. S. Johnson, J. Chem. Phys. **74**, 3791 (1981).
[43] M. Zelikoff, K. Watanabe, and E. C. Y. Inn, J. Chem. Phys. **21**, 1643 (1953).
[44] P. H. Wine and A. R. Ravishankara, Chem. Phys. **69**, 365 (1982).
[45] P. Felder, B. M. Haas, and J. R. Huber, Chem. Phys. Lett. **186**, 177 (1991).
[46] R. Simonaitis, R. Greenberg, and J. Heicklen, Int. J. Chem. Kinet. **4**, 197 (1972).
[47] K. F. Preston and R. F. Barr, J. Chem. Phys. **54**, 3347 (1971).
[48] T. Nakayama, K. Takahashi, Y. Matsumi, N. Taniguchi, and S. Hayashida, J. Geophys. Res. **108**, 4668, DOI:10.1029/2003JD003709 (2003).
[49] S. P. Sander, R. R. Friedl, D. M. Golden, M. J. Kurylo, R. E. Huie, V. L. Orkin, G. K. Moortgat, A. R. Ravishankara, C. E. Kolb, M. J. Molina, and B. J. Finnlayson-Pitts, *Chemical Kinetics and Photochemical Data for the Use in Atmospheric Studies, Evaluation Number 14* (JPL Publications, Pasadena, 2003).
[50] T. Suzuki, H. Katayanagi, Y. Mo, and K. Tonokura, Chem. Phys. Lett. **256**, 90 (1996).
[51] D. W. Neyer, A. J. R. Heck, D. W. Chandler, J. M. Teule, and M. H. M. Janssen, J. Phys. Chem. A **103**, 10388 (1999).
[52] T. Nishide and T. Suzuki, J. Phys. Chem. A **108**, 7863 (2004).
[53] J. M. Teule, G. C. Groenenboom, D. W. Neyer, D. W. Chandler, and M. H. M. Janssen, Chem. Phys. Lett. **320**, 177 (2000).
[54] L. L. Springsteen, S. Satyapal, Y. Matsumi, L. M. Dobeck, and P. L. Houston, J. Phys. Chem. **97**, 7239 (1993).
[55] M. Ahmed, E. R. Wouters, D. S. Peterka, O. S. Vasyutinskii, and A. G. Suits, Faraday Discuss. **113**, 425 (1999).
[56] D. G. Hopper, J. Chem. Phys. **80**, 4290 (1984).
[57] G. E. Busch and K. R. Wilson, J. Chem. Phys. **56**, 3638 (1972).
[58] R. E. Miller and R. O. Watts, Chem. Phys. Lett. **105**, 409 (1984).
[59] Z. S. Huang and R. E. Miller, J. Chem. Phys. **89**, 5408 (1988).
[60] K. Mogi, T. Komine, and K. Hirao, J. Chem. Phys. **95**, 8999 (1991).
[61] M.-P. Gaigeot, P. D. Pujo, V. Brenner, and P. Millié, J. Chem. Phys. **106**, 9155 (1997).
[62] H.-B. Qian, W. A. Herreabout, and B. J. Howard, Mol. Phys. **91**, 689 (1997).
[63] S. Kudoh, K. Onoda, M. Takayanagi, and M. Nakata, J. Mol. Struct. **524**, 61 (2000).

[64] H. Valdes and J. A. Sordo, J. Phys. Chem. A **108**, 2062 (2004).
[65] M. Dehghani, M. Afshari, Z. Abusara, N. Moazzen-Ahmadie, and A. R. W. McKellar, J. Chem. Phys. **126**, 164310 (2007).
[66] C. Maul, M. Poretskiy, A. Rakhymzhan, and J. Grunenberg, J. Mol. Spectrosc. **256**, 80 (2009).
[67] J. Luque and D. R. Crosley, LIFBASE: Database and Spectral Simulation, SRI International Report No. MP 99–009, 1999.
[68] I. Kovacs, *Rotational Structure in the Spectra of Diatomic Molecules* (Adam Hilger, London, 1969).
[69] L. T. Earls, Phys. Rev. **48**, 423 (1935).
[70] J. Luque and D. R. Crosley, J. Chem. Phys. **111**, 7405 (1999).
[71] R. N. Zare, Mol. Photochem. **4**, 1 (1972).
[72] M. W. Chase, Jr., NIST-JANAF Thermochemical Tables, 4th ed., J. Phys. Chem. Ref. Data, Monograph **9** (1998).